University of Bath

Alternative formats
If you require this document in an alternative format, please contact:
openaccess@bath.ac.uk

Investigation of fault modelling in the identification of bearing wear severity

Authors:

Diogo Stuani Alves[1]
Tiago Henrique Machado[1]
Felipe Wenzel da Silva Tuckmantel[1]
Patrick S. Keogh[2]
Katia Lucchesi Cavalca[1]

Address:

[1]Laboratory of Rotating Machinery, School of Mechanic Engineering, UNICAMP
200, Rua Mendeleyev, Campinas, CEP: 13083-860, SP, Brazil.
[2]Department of Mechanical Engineering, University of Bath, Bath BA2 7AY UK

Corresponding Author:

Diogo Stuani Alves
Email: dsalves@fem.unicamp.br

Abstract

Recent research into machines involved in power generation processes has demanded deep investigation of model-based techniques for fault diagnosis and identification. The improvement of critical fault characterisation is crucial in the maintenance process effectiveness, hence in time/costs saving, increasing performance and productivity of the whole system. Consequently, this paper deals with a common fault in hydrodynamically lubricated bearings assembled in rotating systems, namely, that of abrasive wear. Research on this topic points to an interesting query about the significance of model detail and complexity and the identification of its characteristic parameters for the important stages of fault diagnosis and fault identification. For this purpose, two models are presented and analysed in their completeness concerning the fault signature by vibration measurements, as well as the identification of fault critical parameters which determine the machine lifetime estimation, maintenance procedures and time costs regarding performance and productivity. From this study, the detailing in fault modelling has a substantial impact on fault parameter identification, even if its improvement is not so expressive in fault diagnosis procedures involving standard signal processing techniques of vibration signatures.

Keywords: wear, journal bearings, fault identification, rotating systems.

1. Introduction

Rotating machines represent a class of engineering systems with great application in power generation plants, being composed basically of turbines and compressors operating under a wide range of energy sources. These machines involve a considerable number of components, such as bearings, shafts, seals, couplings, and foundations, among others. Hence, critical faults relating to these systems can be diverse in nature, affecting the dynamic response of the machine in different ways. The most common of these faults concern unbalance and misalignment of the

rotating shaft, associated with bearing faults, being responsible for characteristic symptoms in contrast with the usual response of a healthy rotating system.

Many faults detection and identification techniques that have been developed recently use model-based response simulations. In this context, the development of robust and representative models for each component of the rotating system becomes practically a priority, since they are crucial for assessing the machine lifetime and maintenance time costs, directly affecting the performance and productivity of the system.

Concerning the fault parameter identification, recent research has been developed to propose robust techniques for model-based and experimental fault characterisation and its criticality in lubricated journal bearings. When significant wear occurs on the bearing surface over long periods of operation, the need for a new clearance identification method is required. Consequently, the stability of the system, depending on the rotating speed and wear criticality can be also compromised. Inspired by this problem, Papadopoulos et al. [1] developed a theoretical method, using the Finite Element Method (FEM) for radial journal bearings, to identify the radial clearance of worn bearings. In 2011, bearing properties such as eccentricity, attitude angle, hydrodynamic friction and lateral leakage were evaluated as a function of wear depth. To accomplish the numerical simulations, a commercial CFD software was used, and the authors were able to obtain the wear parameters in real-time by graphical identification [2].

Jiang et al. [3] developed a new method for obtaining the severity of faults in rotor dynamic systems. The authors used the FFT to obtain the spectral signal of the time series and used a multi-frequency band method to extract the crucial components of the frequency spectrum. In the same year, Yunusa-Kaltungo [4] proposed a simplified and unified principal component analysis applied to the fault diagnosis of rotating systems. That paper describes a useful approach for improving the reliability in fault diagnosis of identically installed rotating machines, independently of the rotating speed or foundation flexibilities. Two experimental rigs assembled on foundations with different flexibilities were subjected to several rotor-related faults. A data combination method was used to obtain composite higher order spectra, in order to process the fault separation and diagnosis through principal component analysis of the grouped data.

Wang et al. [5] then suggested the use of signal alignment through spectrum phase shifting for multi-fault detection. The main reason for their research is that different fault types require different techniques for their effective detection. However, some detection techniques can be either incapable or ineffective for new fault types. Therefore, a unified signal processing approach was proposed to detect and trend changes caused by different faults sources in rotating machinery. Basically, the procedure involves the extraction of differences between the synchronously averaged signals when subjected to changes in health conditions, by aligning their phases in the frequency domain. Recently, a simulation-based approach was developed to predict the wear profile and location in a connecting rod big end bearing during several crank cycles [6]. The model can yield the main contribution of the wear parameters at different operational conditions. Due to the abrasive nature of the wear, Lee at al. [7] tried to use the pad temperature to detect the presence of wear in tilting-pad bearings. The results showed that the temperature in the loaded pad increases in presence of wear while it decreases if the wear occurs in the unloaded pads.

Recently, Alves et al. [8] presented an analysis using a Convolutional Neural Network (CNN) algorithm to diagnose ovalized journal bearings. The literature involving NN algorithms relies mainly on the need of large amounts of data from physical experiments or from the field, used to training and testing the NN. The paper proposes a condition monitoring model-based strategy based on a deep learning approach to journal bearing fault identification. Therefore, a robust and reliable numerical model is needed to simulate several fault conditions to build the training datasets. Hence, the CNN can be trained with numerical datasets saving time and cost involved in practical tests. At this point, the importance of the parametric representativeness of the fault model becomes crucial.

After the fault is detected and its severity obtained, it is necessary to control the undesirable dynamic effects of the faulty system until the next scheduled maintenance. In these situations,

magnetic actuators and active magnetic bearings (AMBs) are widely used.

Attempts to have a better representation of worn bearings have taken place since the 1980s and it is still an open issue. Dufrane et al. [9] developed the first mathematical representation for worn bearings. The authors targeted the wear mechanics of rotors at low rotating speeds. The experimental observation led to the assumption that the wear was located at the bottom of the bearing. In addition, the wear was considered symmetrical with respect to its maximum depth. Later, Hashimoto et al. [10] used this model to investigate, numerically and experimentally, the effects of geometric changes caused by wear in hydrodynamic bearings.

Some works have been dedicated to causes and consequences in worn bearings. A local thermohydrodynamic analysis of worn bearings was accomplished to observe whether the wear could help oil temperature decrease due to the higher outlet flux [11]. In 2008, an investigation was carried on how friction force, misalignment angles and wear depth could be related in a bearing submitted to high levels of eccentricity, wear and misalignment [12].

Machado and Cavalca [13] enhanced the model of [9] and improved its parametric representation by including a new variable in the wear geometric model. The wear mathematical model was then described in terms of its maximum depth, angular span and angular position in the bearing wall. The authors also proposed directional coordinates to represent the dynamic response of the rotating system. In the same year, Chun and Khonsari [14], using an elastohydrodynamic approach, developed a new equation for the oil film thickness and estimated the wear depth at a bearing used in a single-cylinder engine. The authors stated that the wear occurs during a short period of time during the starting phase of the machine, and during the closing phase of the coast down.

As metal-metal contact occurs in the kinematic shaft-bearing pair during the start-up and coast down of machines, accumulated wear shortens the bearing lifetime. To study this effect, Sander et al. [15] used an elastohydrodynamic model to represent the gradual development of wear during a complete start-stop cycle of an engine's main bearing. Fault parameters such as wear depth and geometrical extent of the wear were related to the shaft movement, contact pressure distribution and lubricant film thickness under shaft angular acceleration.

Vibration signals have an important role in the fault diagnosis and monitoring of rotating machines. Therefore, time responses provide the fundamental information in order to define a general vibration signature in presence of bearing wear. In this context, Machado et al. [16] indicated that a worn bearing excites the backward component (-1x) of the full spectrum in a rotor-bearing system. They used numerical and experimental responses to compare the influence of healthy and worn bearings.

Machado and Storti [17] studied which types of nonlinearities would arise from a rotor vibration response supported by worn bearings. However, there was still an issue to be answered, namely, after the detection of bearing wear, what could be expected in term of fault parameters identification regarding the model-based robustness and reliability? Under this perspective, Alves et al. [18] improved further the model proposed in [13], assuming an elliptical wear geometry with three independent wear parameters: depth, angular span and angular position in the bearing wall. In [18] the authors experimentally validated a new developed wear geometry. The main point, however, was the proposition of a wear identification procedure which needed the vibration signal of a single rotating speed to obtain the wear parameters.

The present paper, advances on [18] by aiming to assess the importance of using broad and reliable fault models to successfully achieve a model-based fault identification. Its unique contribution lies in showing that different fault models can be mathematically effective in the identification process, i.e. both can reach the objective function minimum, however, they might not physically represent the original fault condition. For this, the authors investigate the effects of the inclusion of geometric imperfections, due to the presence of the fault models of wear in two levels of detail, namely, bi-parametric and tri-parametric models. Therefore, the wear models developed in [13] and [18], as well as the identification procedure of [18], are used in this study. The model-based robustness in the fault diagnosis and fault parameter identification is analysed.

Thus, the paper's conclusions can be used for fault prognosis and its criticality in real rotating systems during operation.

2. Theoretical Background

2.1 Hydrodynamic lubrication theory

It is widely known that the Reynolds equation governs the dynamics of journal bearings. This equation, which is obtained from the Navier-Stokes and Continuity equations, subjected to specific assumptions, has become the foundation of the classical hydrodynamic lubrication theory, its solution provides the pressure distribution in the lubricating fluid:

$$\frac{1}{R^2}\frac{\partial}{\partial \theta}\left(h^3\frac{\partial p}{\partial \theta}\right) + \frac{\partial}{\partial x}\left(h^3\frac{\partial p}{\partial x}\right) = 6\mu\left(\Omega\frac{\partial h}{\partial \theta}\right) + 12\mu\frac{\partial h}{\partial t}. \tag{1}$$

in which, θ and x represent the circumferential and axial coordinates, R is the journal bearing radius, Ω is the shaft rotating speed, p is the lubricant film pressure, μ is the oil viscosity, t is time and h is the oil film thickness, which can be written, for a bearing without wear, as:

$$h_0(\theta) = C + e_y \sin\theta - e_z \cos\theta, \tag{2}$$

where e_y and e_z are, respectively, a decomposition of the eccentricity ratio, e, in y and z directions and C is the bearing radial clearance. Figure 1 shows a generic schematic of a cylindrical bearing.
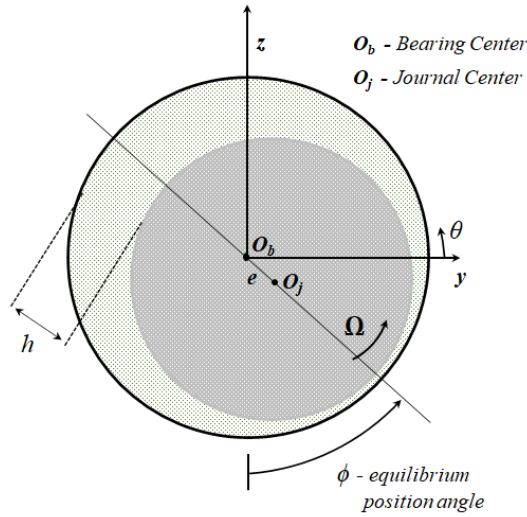

Figure 1: Schematic bearing.

The presence of wear on the inner surface of the bearing changes the oil film thickness. Therefore, discontinuities in the oil film thickness, and consequently, in the radial clearance, might appear. To overcome this issue, the procedure proposed in [19] for unidimensional cases and expanded to bi-dimensional problems by [13], is used to solve the Reynolds equation in the presence of a discontinuous oil film.

The Reynolds equation is a second-order partial differential equation. Consequently, its complete solution, which gives the pressure distribution on the oil film, is achievable only through numerical methods. The Finite Volume Method (FVM) is selected for this task. FVM

approximates a system of differential equations by a system of discrete algebraic equations, in which the number of discrete equations is equal to the number of finite volumes in the numerical mesh [20].

Once the pressure distribution is evaluated, it is possible to obtain the hydrodynamic force components (f_{Hy} and f_{Hz}) through the integration of pressure distribution, i.e.:

$$f_{Hy} = \int_{-\frac{L}{2}}^{\frac{L}{2}} \int_{\theta_1}^{\theta_2} p \sin\theta \, Rd\theta dx \; ,$$

$$f_{Hz} = -\int_{-\frac{L}{2}}^{\frac{L}{2}} \int_{\theta_1}^{\theta_2} p \cos\theta \, Rd\theta dx \; . \tag{3}$$

2.2 Wear modelling

Worn bearings are usually modelled with abrasive wear, caused by several rotor starts and stops and/or contact between the bushing and journal during high whirling motion [9], taking account of changes in oil film thickness due to the presence of wear, i.e., the changes that will affect the pressure distribution, hydrodynamic forces and, consequently, the dynamics of the rotor. It was beyond the scope of [9] to develop a model for the wear mechanism. However, [9] considered the wear as symmetric and fixed at the bottom of the bearing, where the maximum wear depth is located. Moreover, the wear model has a constant depth in the axial direction (x), and the angular extent is dependent on the maximum wear depth. To improve the model parametrisation, [13] introduced a new degree of freedom into the problem, which enables positioning the maximum depth at any angular position on the bearing surface. This degree of freedom is represented by the variable γ, as shown in Fig. 2a.
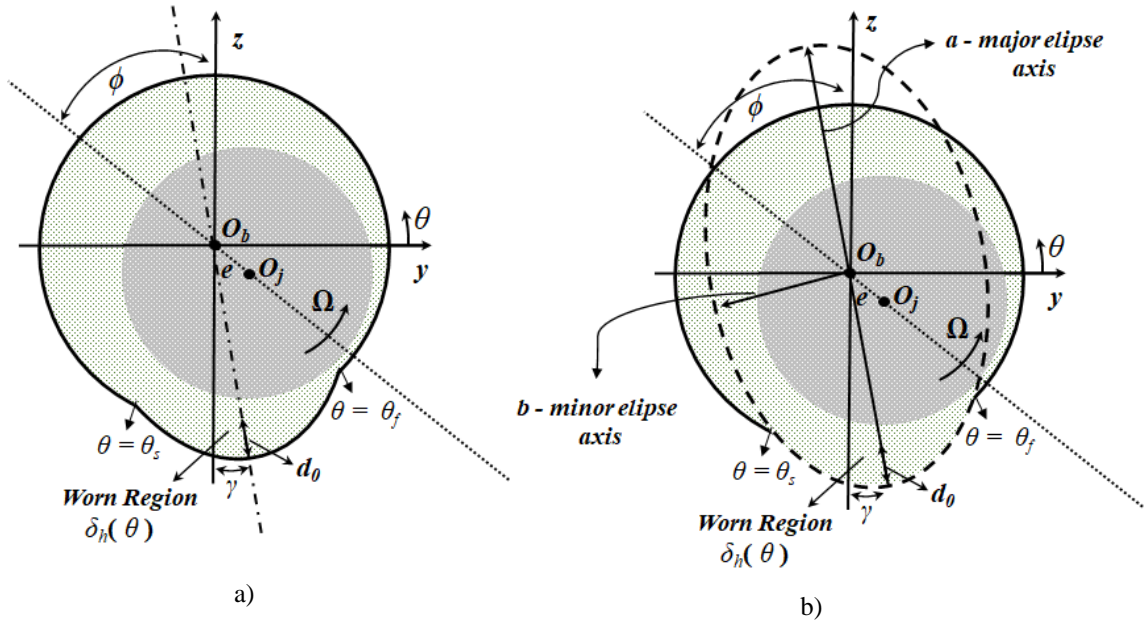

Figure 2: Wear representation in the bearing geometry: a) Wear model proposed in [13]. b) Wear model proposed in [18].

Therefore, the oil film thickness in a worn bearing is given by:

5

$$h(\theta) = h_0(\theta) + \delta_h(\theta), \tag{4}$$

which includes δ_h to increase the oil film thickness caused by the wear, mathematically written as:

$$\delta_h(\theta) = d_0 - C\left[1 + \cos\left(\theta - \frac{\pi}{2}\right)\right], \tag{5}$$

where d_0 is the maximum wear depth.

The initial (θ_s) and final (θ_f) angular span of the wear can be found by setting the wear depth $\delta_h(\theta)$ to zero. Hence:

$$\cos\left(\theta - \frac{\pi}{2}\right) = \frac{d_0}{C_r} - 1,$$

Then, introducing the angular displacement γ into the problem, one can find:

$$\theta_s = \frac{\pi}{2} + \cos^{-1}\left(\frac{d_0}{C_r} - 1\right) + \gamma;$$

$$\theta_f = \frac{\pi}{2} - \cos^{-1}\left(\frac{d_0}{C_r} - 1\right) + \gamma. \tag{6}$$

Therefore, the total oil film thickness can be finally written as:

$$h(\theta) = \begin{cases} h_0(\theta), & 0 \le \theta \le \theta_s, \theta_f \le \theta \le 2\pi \\ h_0(\theta) + \delta_h(\theta), & \theta_s \le \theta \le \theta_f \end{cases}. \tag{7}$$

However, as previously stated, the angular span of the wear is dependent on the maximum wear depth. An expansion in the parametric wear model [18] is introduced in which there is no relation between angular span and maximum depth, i.e., these parameters are completely independent variables. The authors used an elliptical shape to approach the wear geometry, as presented in Fig 2b. The intersection points between the ellipse and the bearing radius define the initial and final wear angular span. Eqs. (8) and (9) show the ellipse and circle equations centred at O_b:

$$\frac{y^2}{a^2} + \frac{z^2}{b^2} = 1 \Rightarrow y^2 = \frac{a^2}{b^2}\left(b^2 - z^2\right), \tag{8}$$

$$y^2 + z^2 = r_b^2. \tag{9}$$

Solving Eq. (8) in Eq. (9) simultaneously, one has:

$$z = \pm\sqrt{\frac{b^2\left(r_b^2 - a^2\right)}{b^2 - a^2}} \text{ and } y = \pm\sqrt{r_b^2 - \frac{b^2\left(r_b^2 - a^2\right)}{b^2 - a^2}} \tag{10}$$

However, it is interesting to write the equations in terms of the maximum wear depth d_0, angular position of the maximum wear depth γ and wear angular span $\beta = \theta_f - \theta_s$ instead of the ellipse radii a and b.

Since $\theta_s = \frac{3\pi}{2} - \frac{\beta}{2} + \gamma$, $d_0 = b - r_b$ and taking the canonical forms:

$$y = a\cos(\theta), \tag{11}$$

$$z = b\sin(\theta), \tag{12}$$

one can obtain: $a = \sqrt{\dfrac{r_b^2 - b^2\sin^2(\theta_s)}{1 - \sin^2(\theta_s)}}$.

Finally, the extra oil film thickness created by the elliptical wear is:

$$\delta_h = \sqrt{y^2 + z^2} - r_b = \sqrt{a^2\cos^2(\theta') + b^2\sin^2(\theta')} - r_b, \tag{13}$$

in which $\theta' = \theta + \gamma$. The complete oil film thickness is still given by Eq. (4).

2.3 Magnetic bearing modelling

Active magnetic bearings are designed to generate contact-free forces by controlling the rotor levitation and dynamics by varying the coil currents. They provide reaction forces for the weight of the rotor and can also control its position and vibration. In addition, they can also be used as vibration exciters, sensors and actuators [21]. Therefore, magnetic bearings can help improve rotor dynamic behavior by introducing new features in the identification, diagnosis and optimization techniques.

In this context, Cole et al. [22] developed a fault-tolerant control and a fault identification method, based on neural networks, for rotating systems supported on active magnetic bearings. Dimitri et al. [23] controlled oil whip instability using a magnetic bearing as an actuator and by implementing an H_∞ controller. This approach has been transformed into an integrated magnetic/journal bearing by El-Shafei [24]. Analysing the full spectrum of the displacement and active magnetic bearing currents, Sarmah and Tiwari [25] proposed a method to identify cracks in shafts. Current stiffness and displacement stiffness are key parameters of a magnetic bearing. Through a new dynamic stiffness measurement method, Sun et al. [26] analysed the changes of those two parameters in magnetically suspended molecular pumps at high rotating speeds.

In this paper, magnetic bearings are used as controllable auxiliary subsystems to place the rotor at a specific operating point" during the wear assessment of journal bearings. Therefore, the magnetic bearings used here have opposing coil pairs located at ±45º from the vertical axis z.

Consequently, the vectorial sum of the forces developed by the coils gives the total force generated by the magnetic bearings. Since this is an opposing pair configuration, one of the magnets depends on the control current i_c added to the bias current i_1 ($i_1 + i_c$), while the opposing one depends on the control current subtracted from its bias current i_2 ($i_2 + i_c$) (Figure 3). So, a single control axis force of the magnetic pair can be calculated as [27]:

$$F_{MZ} = \frac{\mu_0 A N_c^2 (i_1 + i_c)^2}{\left[\dfrac{l_i}{\mu_r} + 2(l_0 - z) \right]^2} \cos(\theta) - \frac{\mu_0 A N_c^2 (i_2 - i_c)^2}{\left[\dfrac{l_i}{\mu_r} + 2(l_0 + z) \right]^2} \cos(\theta) \tag{14}$$

where μ_0 the relative permeability of free space, A the pole face area, N_c the number coil windings, 2θ the polar angle of the coil, l_i the path length through the coil core, μ_r the relative permeability of the magnetic core, z the shaft displacement in the vertical direction and l_0 the air gap when $z = 0$.
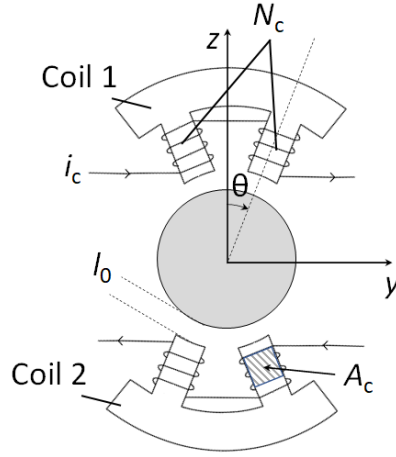

Figure 3: Magnetic bearing scheme.

By introducing a bias current, it is possible to set the rotor at an appropriate operating point, and also to linearize Eq. (14) around $z = 0$ and $i_c = 0$ leading to:

$$F_{MZ} = -k_z z + k_i i_c \tag{15}$$

in which k_z is known as the negative stiffness:

$$k_z = \frac{4\mu_0 A N_c^2 (i_1^2 + i_2^2)}{\left(\dfrac{l_i}{\mu_r} + 2l_0 \right)^3} \cos(\theta) \tag{16}$$

and k_i is known as current gain:

$$k_i = \frac{2\mu_0 A N_c^2 \left(i_1 + i_2 \right)}{\left(\dfrac{l_i}{\mu_r} + 2l_0 \right)^2} \cos(\theta) \tag{17}$$

For the given magnetic bearings, the negative stiffness and current gain are, respectively, $k_z = 1.94 \times 10^6$ N/m and $k_i = 530$ N/A. These values were previously obtained in the experiments accomplished in [27]

Applying the same procedure to the horizontal and vertical directions, one obtains the magnetic force in vector-matrix form as:

$$\mathbf{f}_M = -\mathbf{K}_z \mathbf{q} + \mathbf{K}_i \mathbf{i}_c \tag{18}$$

A relatively standard method to control a rotor in a magnetic bearing is to use proportional-integral-derivative (PID) feedback of measured rotor lateral displacements. The proportional gain is used to overcome negative stiffness and to provide a positive stiffness to the rotor. The integral gain is used to achieve a desired steady state position (eccentricity) of the rotor. The derivative gain is used to provide a suitable level of damping to the rotor. In this case, Eq. (19) shows the expression for the control current:

$$\mathbf{i}_c = \frac{1}{k_i} \left(\mathbf{K}_P \mathbf{q} + \mathbf{K}_I \int_0^t \mathbf{q} \, dt + \mathbf{K}_D \dot{\mathbf{q}} \right) \tag{19}$$

in which the matrices are diagonal with common elements $K_P = 3 \times 10^6$ N/m, $K_I = 3 \times 10^5$ N/s/m and $K_D = 5 \times 10^3$ Ns/m, respectively, as proportional, integral and derivative gains. Detailed information about control and magnetic bearings properties and functioning is given in [28].

Moreover, the magnetic bearing used in the current paper presents linear behaviour until it reaches a force of approximately ±1500 N around the centre of the bearing [27]. In addition, for the analysis given here, the vibration in not excessively high in order to need control forces that will surpass the linearity limit. Thus, the application of linear magnetic bearings is accurate for the analysed conditions.

2.4 Rotating system modelling

Traditionally, the FEM is used to represent the rotating system rotor dynamics. In this paper, a rotor is supported by two active magnetic bearings (AMB) and one hydrodynamic bearing, placed at nodes 7, 19 and 25 respectively. Figure 4 depicts a schematic of rotor studied while Table 1 gives the elements details. Using the FEM, it is possible to approximate a continuum system by several continuum elements. Using the rotor nodal displacements, one can compute the energy of Timoshenko beam elements and use Lagrange's equations to obtain the system equation of motion [29]:

$$\mathbf{M}\ddot{\mathbf{q}}(t) + (\mathbf{C} + \Omega \mathbf{G})\dot{\mathbf{q}}(t) + \mathbf{K}\mathbf{q}(t) = \mathbf{f}(t), \tag{20}$$

where $\mathbf{M}$, $\mathbf{C}$, $\mathbf{G}$ and $\mathbf{K}$ are the global mass, damping, gyroscopic and stiffness matrices; $\mathbf{f}(t)$ is the

vector containing external forces and $\mathbf{q}(t)$ the degree of freedom vector. The damping matrix is assumed proportional and it is dependent on mass and stiffness matrices, as follows:

$$\mathbf{C} = \alpha_1\mathbf{M} + \alpha_2\mathbf{K}, \tag{21}$$

where $\alpha_1 = 0$ and $\alpha_2 = 1.5\times10^{-5}$ are, respectively, the mass and stiffness proportionality coefficients.
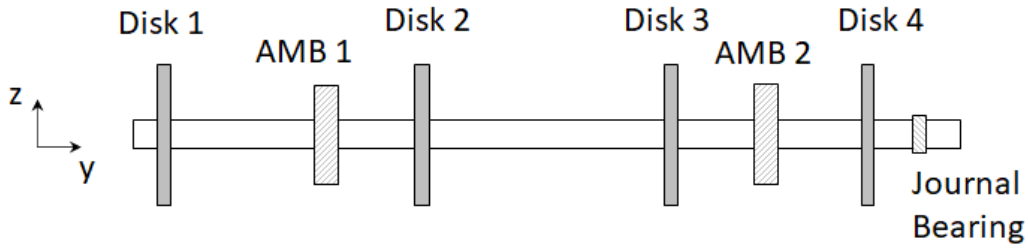

Figure 4: Rotating system: shaft modelled by Timoshenko beam elements.

Table 1: Element details.

Element number	Element type	Internal diameter [mm]	External diameter [mm]	Length [mm]	Material
1	Beam	0	50	62.5	Steel
2, 3	Beam	0	150	17.5	Steel
4	Beam	0	50	193.5	Steel
5	Beam	0	50	179	Steel
6, 7	Beam	0	50	30	Steel
8	Beam	0	50	37.1	Steel
9, 16	Beam	0	50	161	Steel
10, 11	Beam	0	150	17.5	Steel
12	Beam	0	50	304.1	Steel
13	Beam	0	50	303.8	Steel
14, 15	Beam	0	150	17.5	Steel
17	Beam	0	50	36.6	Steel
18, 19	Beam	0	50	30	Steel
20	Beam	0	50	215.7	Steel
21, 22	Beam	0	150	17.5	Steel
23	Beam	0	50	94	Steel
24, 25	Beam	0	67	20	Steel
26	Beam	0	50	86.1	Steel
27, 28, 29, 30	Disk	150	250	35	Steel

31, 32	Disk	50	175.4	60	Aluminium + Steel

Therefore, the rotating system is composed of a steel shaft having elasticity modulus $E = 215$ GPa and density $\rho = 7800$ kg/m^3, divided into 26 Timoshenko beam elements. Two AMBs located at nodes 7 and 19, and one hydrodynamic journal bearing located at node 25, support the rotor, as presented in Figure 4. Also, four steel disks, modelled as rigid elements, are placed at nodes 3, 11, 15 and 25. Finally, the AMB journals are assembled as aluminium and laminated steel composites, located at the AMB positions, with an equivalent density $\rho = 5250$ kg/m^3.

Both magnetic and hydrodynamic bearing dynamics are inserted in the rotating system model by means of forces. Hydrodynamic bearings forces, given in Eq. (3), are usually linearised through a first-order Taylor series expansion around the journal equilibrium position. Thus, it is possible to represent the bearing through stiffness and damping coefficients, as proposed by Lund [30]. The linearised forces for a given equilibrium position are:

$$f_{Hy} = f_{Hy0} + K_{yy} \cdot \Delta y + K_{yz} \cdot \Delta z + C_{yy} \cdot \Delta \dot{y} + C_{yz} \cdot \Delta \dot{z},$$

$$f_{Hz} = f_{Hz0} + K_{zy} \cdot \Delta y + K_{zz} \cdot \Delta z + C_{zy} \cdot \Delta \dot{y} + C_{zz} \cdot \Delta \dot{z},$$

(22)

in which, the coefficients are calculated by the partial derivatives evaluated at the equilibrium position, for each rotating speed of the shaft:

$$K_{ab} = \left.\frac{\partial f_{Ha}}{\partial b}\right|_{(x_0,y_0)}; \quad C_{ab} = \left.\frac{\partial f_{ha}}{\partial \dot{b}}\right|_{(x_0,y_0)}.$$

(23)

Similarly, the AMBs are also commonly represented by springs and dampers. The direct coefficients can be easily determined using the proportional and derivative gains (K_P, K_D) of the control law, Eq. (19). However, for radial magnetic bearings, the cross-coupling effects, i.e., those effects related to the integral gain K_I, are assumed to have negligible influence on the rotor dynamics. Therefore, for AMB1: $K_{AMB1yy} = K_{AMB1zz} = 0.848 \times 10^6$ N/m and $C_{AMB1yy} = C_{AMB1zz} = 4000$ Ns/m. On the other hand, for AMB2: $K_{AMB1yy} = K_{AMB1zz} = 1.272 \times 10^6$ N/m and $C_{AMB1yy} = C_{AMB1zz} = 6000$ Ns/m.

2.5 Wear identification

Model-based identification of faults relies on optimisation procedures to find the best fault configuration that satisfies necessary and sufficient conditions. Therefore, one should choose the variables and objective function wisely to correctly represent the fault characteristics.

For the wear identification presented in this paper, fault variables used in the optimisation process comprise the maximum wear depth (d_0), angular position of the maximum depth (γ) and angular span of the wear (β). If the identification is accomplished using the two-parameter wear model, only the first two variables are necessary because the angular span is dependent on the maximum depth. Otherwise, all parameters are included in the optimisation.

Since the goal of model-based identification is to estimate the fault severity in a real machine

using mathematical models, the objective function must consider a comparison between the physical and numerical system responses. Thus, measured data are mandatory for identifying the severity of any kind of fault. When considering rotor dynamic systems, the most common points for acquiring measurements are the bearing positions. In this situation, the displacement of the shaft inside or near the bearing, as well as bearing house accelerations, are commonly used. Since modifications in the values of the wear parameters change the bearing dynamic behaviour and, consequently, the rotor dynamic behaviour, the shaft displacements inside the bearings are the best ones to be monitored.

Instead of using the raw vibration data in the time domain, this paper uses the full-spectrum, through the Discrete Fourier Transform (DFT) of the time series. The information in the spectral domain presents all harmonic components of the original signal. Thus, it is easier to recognise specific dynamics characteristics of the faulty rotor and, consequently, fault signatures. Therefore, to estimate the difference between experimental and numerical spectra data, the least-squares formulation is recommended:

$$f(t, d_0, \gamma, \beta) = \frac{1}{2} \left\| \mathbf{DFT}(\mathbf{q}(t, d_0, \gamma, \beta)) - \mathbf{DFT}(\overline{\mathbf{q}}(t)) \right\|_2^2, \tag{24}$$

where $\overline{\mathbf{q}}(t)$ are the experimental time series data.

Then, the model-based identification of the wear becomes an optimisation problem that aims to minimise the difference between numerical and experimental vibrations by varying the geometric wear parameters in the numerical model. This problem can be written in the more general form as:

$$\begin{aligned} \min_{s.t.} \quad & f(t, d_0, \gamma, \beta) = \frac{1}{2} \left\| \mathbf{DFT}(\mathbf{q}(t, d_0, \gamma, \beta)) - \mathbf{DFT}(\overline{\mathbf{q}}(t)) \right\|_2^2 \\ & 0 \le d_0 \le d_{0\max} \\ & \gamma_{\min} \le \gamma \le \gamma_{\max} \\ & \beta_{\min} \le \beta \le \beta_{\max} \end{aligned} \tag{25}$$

in which, $d_{0\max}$, $\gamma_{\max}$ and $\beta_{\max}$ are the maximum values imposed on the wear main parameters and, analogously, $\gamma_{\min}$ and $\beta_{\min}$ are the minimum values imposed on these variables.

Since Eq. (25) presents a nonlinear objective function, it is classified as a constrained Nonlinear Programming Problem (NLP) and any, deterministic or heuristic, optimisation method developed for this class of problems can solve it. For the present paper, the gradient-based technique known as the Barrier Method (BM) is used, which approximates a constrained optimisation in a series of unconstrained optimisations [31]. The unconstrained problem solution, which becomes the minimisation of a least square formulation, is achievable by the method presented by Dennis and Schnabel [32] in conjunction with the Wolf Conditions [33]. A detailed description of the adopted optimisation procedure can be found in [18].

Some similar methods used for wear identification are presented by [1], [13] and [33]. In Dufrane's work [1], the objective function is calculated using the differences between the simulated and experimental equilibrium positions at a given location of the rotor. However, despite the efficiency of proximity probes in measuring rotor vibrations, experimental journal loci are not easily determined in uncontrolled environments, such as occurring in real machines. Machado et al. [13] used information of the numerical and experimental unbalance response to obtain the wear parameters. Regardless of having good results, this method needs vibration data

from several rotating speeds, which are not usually available from machines in the field. Finally, Mendes et al. [34] used information from the frequency response function (FRF) to identify wear geometry. Although the procedure is effective, some sort of external excitation would be necessary to obtain the real FRF, making its use less attractive in many situations. Therefore, the method proposed by Alves et al. [18] is the one that uses monitoring information already available in any rotating machine, i.e., the vibration at the bearing positions, and it only requires this information at a single operating condition.

A Design of Experiments (DOE) was performed to improve the chances of finding a global minimum. The set of variables that has the lower objective function is selected as the starting point for the optimisation procedure.

3. Test Rig Description

The experimental rotating system shown in Figure 5 is composed by a stainless-steel shaft, four stainless-steel disks, two radial magnetic bearings and one radial hydrodynamic bearing. The shaft has a diameter of 50 mm and is approximately 2 m long. On this shaft, four disks are assembled, which are 35 mm wide and have a diameter of 250 mm. In addition, the disks have threaded holes spaced 22.5º from each other and located at 100 mm from the centre of the disk, which enables the addition of balance and unbalance masses.

The active magnetic bearings (AMB1 and AMB2) both have an axial length of 60 mm, a diameter of 177.8 mm and an air gap of 1.2 mm. To prevent any sudden failure, touch-down bearings, with 0.7 mm of radial clearance, are mounted on the inboard side of each AMB. Moreover, the AMBs are composed of 8 poles. The hydrodynamic bearing used to support the experimental rotor is 38 mm wide, having a diameter of 67.38 mm and a radial clearance of 185 μm. Since the shaft diameter has a considerably smaller diameter than the bearing bores, journals were assembled at their locations to achieve the desired clearances. Furthermore, to supply Castrol ASW 32 oil to the journal bearing, a tank was placed at 1.5 m above the test rig, allowing the lubricant to flow to the bearing by gravity action. At this height, the inlet pressure is about 1.15 bar.
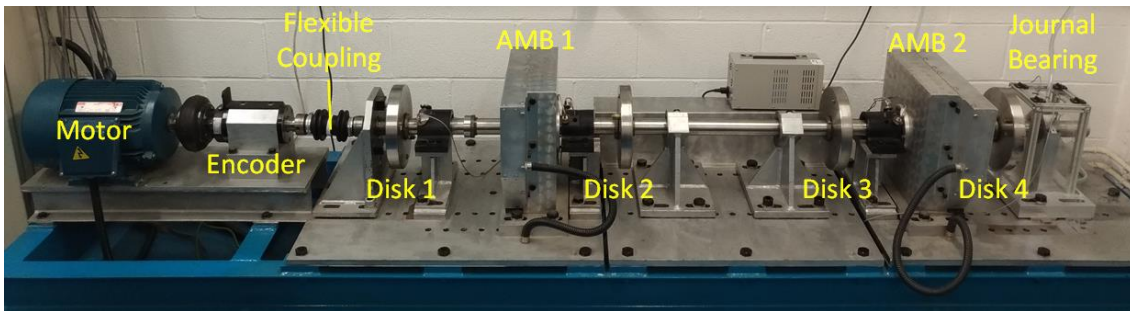

Figure 5: Test rig configuration.

To connect the rotor to the Alpak 5.5 kW induction motor, a flexible coupling, which allows radial and angular misalignments between motor and rotor, is used. Moreover, an encoder from British Encoder (model 776-HV), placed between the motor and flexible coupling and used as a key phasor and to determine the instantaneous rotating speed. Six Sensonics XPR04 eddy current proximity probes, rotated by ±45º in respect to the vertical direction, were inserted at the journal bearing and near the AMB positions for acquiring displacement signals. Their measuring range is from 0 to 2.5 mm with a resolution less than 1 μm, and nominal sensitivity of 7.87 V/mm ± 1%.

The signals coming from the proximity probes pass through a signal conditioner before feedback to a dSPACE controller board. Using the measured displacement data, the programmed AMB controller calculates the magnetic force values, which are set by coil current demand values to the AMB power amplifiers.

During the tests, 5 s of displacement data, at a sampling frequency of 2.4×10^{-4} Hz, were acquired by the proximity probes at the journal bearing and near the AMBs positions. The signals were collected 5 times to reduce the effects of variance in the results. Therefore, the post-processing uses the average value of the displacements. In addition, a Butterworth band-pass digital filter, which the highest admitted frequency was 100 Hz and the lowest 5 Hz, was used to digitally filter the acquired vibrations.

Moreover, the rotor was initially balanced, and 5 g unbalance masses were then placed at 100 mm from the centre of each disk. Therefore, there are four unbalance masses in the system, which are the source of harmonic excitation. Moreover, the unbalance masses at the left and right ends of the rotor are 190º out of phase to those on the central disks.

4. Results and Discussion

Besides the choice of which variables and objective function should be adopted, another crucial point for a successful model-based fault identification is a reliable mathematical model of the rotating system and the fault condition. Therefore, the first step in an experimental procedure is to validate the rotor numerical model. For this purpose, the numerical and experimental unbalance responses are compared.

Since the mathematical model can only reproduce vibrations that come exclusively from the unbalance excitation, the differences between signals acquired using the balanced and unbalanced rotors were used as experimental data. This procedure aims to mitigate possible influences of non-linearities in the system, small misalignments at the coupling and electrical and mechanical runout. The experiments were then repeated for three different worn bearing conditions. Table 2 details the wear levels used in terms of model parameters.

Table 2. Physical wear geometries.

	d_0 [μm]	γ [º]	β [º]
Wear 1	46.5	23	77
Wear 2	98.28	5.1	74
Wear 3	15.02	19	102

The mathematical model proposed in section 2.4 was used in this comparison. To recreate the conditions of the experimental tests, the same unbalance masses were placed at nodes 4, 10, 14 and 21, which correspond to their positions in the physical rotor.

The choice of AMBs to support the rotor is advantageous. This type of bearing can reduce, or even suppress, some rotor dynamic effects that are not considered in the mathematical model, such as misalignment. Another advantage of using AMBs is to set the shaft at a specific position inside the journal bearing. So, for experimental and numerical tests the journal static position was maintained initially at an eccentricity ratio of approximately 0.1, and afterwards at an eccentricity ratio of approximately 0.7.

Since the paper aims to discuss the importance of using an accurate fault model, only displacement data collected at the journal bearing position were analysed. Moreover, the wear fault is on the bearing's inner surface. Therefore, the rotor behaviour will be affected mainly at and near this position, which justifies the aforementioned decision.
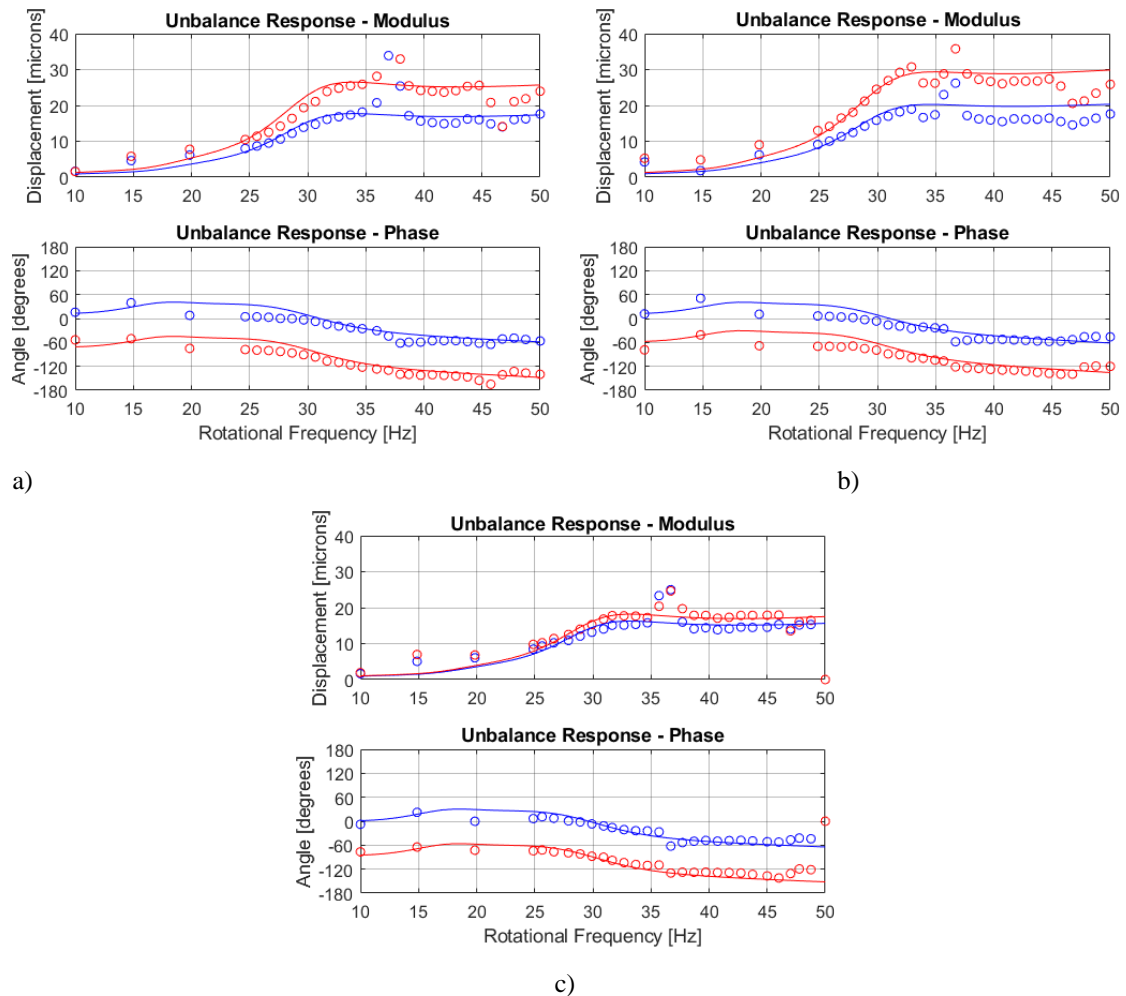
Figure 6: Rotor unbalance response at hydrodynamic bearing position. Bearing having: a) Wear 1. b) Wear 2. c) Wear 3.

Figure 6 shows the rotor unbalance response at the journal bearing position between 10 Hz and 50 Hz for the situations in which the journal bearing presents wears 1, 2 and 3. In this operating range, it is possible to state that the mathematical models and experimental results are in good agreement, both in trends and magnitudes. It is important to say that the three-parametric wear model was used for these comparisons. Moreover, the first critical speed of the system is around 31 Hz. However, there is a second resonance around 37 Hz that is not predicted. This vibration effect is attributed to the base plate or bearing pedestals, which are not accounted for in the model. Moreover, it is possible to verify an increase of the displacements when the wear becomes more severe, as well as an increase in bearing anisotropy, given by the different amplitudes of the Y and Z directions.

Once the numerical results show the model can properly reproduce the experimental test with acceptable accuracy, it is possible to proceed to the next analyses, to assess the representativeness of the wear fault model. Therefore, using both presented wear models, an identification of the wear severity is accomplished for three different levels of wear. In addition, the rotating speed of 34 Hz, which is above the first critical speed, is chosen for this procedure.

To obtain worn bearings physically, a wear configuration was selected, and the pattern was machined on the inner surface of the bearing. Wear 1 was selected to maintain the proportionality between wear depth and angular span as initially proposed by [9] and [13]. Wear 2 has deep wear with relatively small angular extent, while Wear 3 presents shallow wear with large angular extension [18].

Table 3. Identified wear parameters for eccentricity of 0.1.

	Three parameters model			Two parameters model		
	d_0 [μm]	γ [°]	β [°]	d_0 [μm]	γ [°]	β [°]
Wear 1	45.5 ± 0.72	27.87 ± 0.15	82.43 ± 0.55	45.27 ± 0.40	26.95 ± 0.74	80.61 ± 1.03
Wear 2	107.14 ± 0.53	5.34 ± 0.07	68.11 ± 0.05	53.27 ± 0.21	4.69 ± 0.13	89.97 ± 0.19
Wear 3	14.95 ± 0.27	16.86 ± 0.89	102.14 ± 8.87	15.31 ± 0.18	20.56 ± 3.02	47.34 ± 0.13

Table 4. Identified wear parameters for eccentricity of 0.7.

	Three parameters model			Two parameters model		
	d_0 [μm]	γ [°]	β [°]	d_0 [μm]	γ [°]	β [°]
Wear 1	50.11 ± 0.49	23.51 ± 0.72	70.10± 0.85	48.66 ± 0.18	22.66 ± 0.10	85.04 ± 0.10
Wear 2	104.41 ± 0.37	7.46 ± 0.60	68.17 ± 0.59	44.64 ± 0.07	4.10 ± 0.01	82.03 ± 0.01
Wear 3	13.76 ± 0.67	21.51± 1.97	94.76± 2.00	16.95 ± 0.61	21.92 ± 0.99	49.42 ± 0.92

Comparing and minimising the difference between the rotor displacement obtained through numerical simulation and experimental measurements at the journal bearing position, it is possible to identify the wear severity level. DFT values appropriate to the forward 1x and backward -1x components were accounted for by the optimisation. These components are the most affected in the presence of wear, as observed by [16].

To increase the likelihood of achieving a global minimum, a DOE is performed before the identification process. For this, a numerical grid was created, in which the limits were the minimum and maximum imposed values for the wear variables. The variable combination that presents the lowest objective function value was selected as the initial condition.

Table 5. Error in the wear parameters identification for eccentricity of 0.1.

	Three-parameter model			Two-parameter model		
	d_0 [%]	γ [%]	β [%]	d_0 [%]	γ [%]	β [%]
Wear 1	-2.15 ± 1.55	21.17 ± 0.66	7.05 ± 0.72	-2.64 ± 0.86	17.17 ± 3.22	4.69 ± 1.34
Wear 2	9.02 ± 0.54	4.90 ± 1.38	-7.96 ± 0.07	-45.80 ± 0.22	-8.04 ± 2.55	21.58 ± 0.26
Wear 3	-0.47 ± 1.80	-11.26 ± 4.69	0.14 ± 8.70	1.93 ± 1.56	8.21 ± 15.85	-53.58 ± 0.13

Table 6. Error in the wear parameters identification for eccentricity of 0.7.

	Three-parameter model			Two-parameter model		
	d_0 [%]	γ [%]	β [%]	d_0 [%]	γ [%]	β [%]
Wear 1	7.76 ± 1.05	2.22 ± 3.13	-8.96 ± 1.10	4.64 ± 1.03	-1.48 ± 0.50	10.44 ± 0.13
Wear 2	6.24 ± 0.37	46.27 ± 11.76	-7.88 ± 0.79	-54.58 ± 0.22	-19.61 ± 0.78	10.85 ± 0.02
Wear 3	-8.39 ± 4.46	13.21 ± 10.36	-7.10 ± 1.96	12.85 ± 5.06	15.36 ± 5.21	-51.54 ± 0.90

In order to analyse the influence of the initial condition on the final optimised parameters, each wear identification was processed five times with different starting points. These points were obtained by the previously mentioned DOE procedure. However, the grid size for each variable was increased sequentially from four to eight points. The idea was to evaluate the robustness of the identification method, eliminating the dependence on the optimisation starting point. In this way, it is possible to evaluate not only the wear models but also the search method. Tables 3 and 4 show the identified parameters in terms of mean values and standard deviations for the eccentricities of 0.1 and 0.7, respectively, while Tables 5 and 6 presents the errors of identified parameters compared to physical wear parameters in each fault condition, again for the eccentricities of 0.1 and 0.7.

It is possible to see in Tables 3 to 6 that the identification procedure is satisfactory for all cases when the three-parameter wear model is used, predicting, in general, errors smaller than 10% for the wear depth. Regarding the wear angular position (γ), even though the greatest error is around 45%, when dealing with angular magnitudes in degrees, these differences are not excessive, being about 4° to 5°, which is a small absolute error considering the actual location of the wear central point. Finally, for the angular extent, errors smaller than 9% were found, showing a great accuracy of the method for this variable.

It is possible to say that the wear parameters have been identified at both eccentricities with reasonable success. However, the associated errors are slightly higher when the identification happens at an eccentricity of 0.7. In this situation, the dynamics predicted by the computational model do not correlate as well as when the rotor is at an eccentricity of 0.1, introducing further difficulties for the optimisation and culminating in slightly higher errors.

When the two-parameter model is selected to represent the bearing fault, only Wear 1 can be correctly predicted, since Wear 2 and Wear 3 have no correlation between wear depth and wear angular extent. Furthermore, observing Tables 5 and 6, small standard deviations for the identified parameters are evident, showing that the optimisation is not severely influenced by the initial condition. Also, Wear 2, which is the deepest wear condition studied, presents the smallest standard deviations, and as the wear depth decreases, the standard deviation increases. Thus, one can say that it is more difficult to correctly identify shallow wears, once the changes in the rotor dynamics caused by this wear geometry are insignificant when compared to deeper wears.

These results show two points. First, the importance of a robust method capable of identifying the parameters consistently, by minimising the difference between experimental and numerical model responses, regardless of the initial condition. Second, the need of a representative model for the fault under analysis, because, despite the method proving to be robust for the minimisation, it can achieve parameter values quite far from reality, even when the objective function has been satisfactorily minimised (identification of the Wear 1 and 2 for the two-parameter model).

Figures 7, 8 and 9 show the experimental and numerical DFT full-spectrum responses, calculated using the mean values of the wear parameters for both models and for wear conditions 1, 2 and 3. Since results would be analogous, only the information regarding the eccentricity of 0.1 was used

for this analysis. In these figures, there are markers indicating the data values of the 1x and -1x frequency components. The markers to the left of each component are related to the numerical responses, while the ones to the right are related to the experimental curves. Observing the spectral response of the displacement, it is once again possible to verify the vibration amplitude increase - i.e., increase of the forward 1x component – and anisotropy change (noticed through changes in the backward -1x component), as observed in the unbalance response.
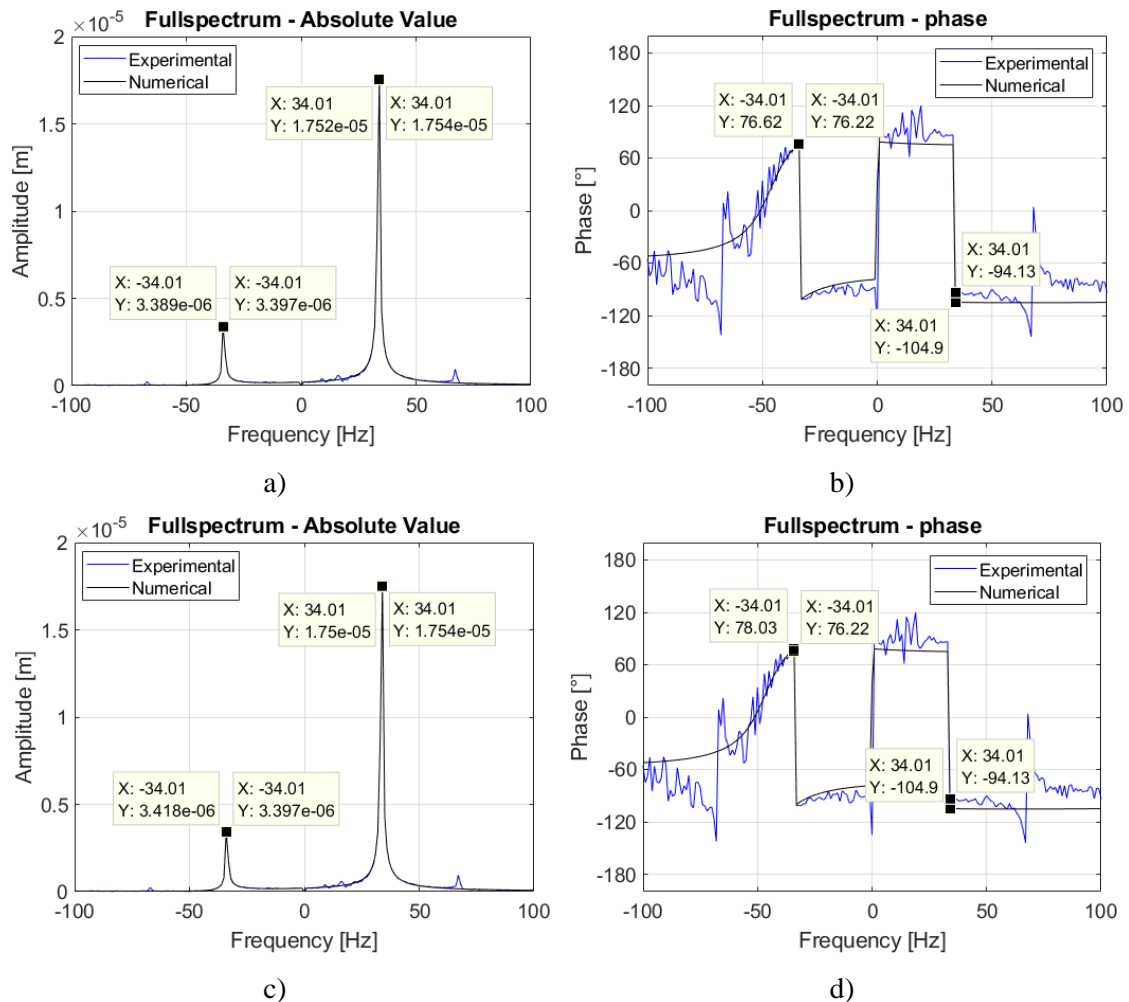
Figure 7 – Wear 1 DFT full-spectrum response: a) Three-parameter amplitude values. b) Three-parameter phase values. c) Two-parameter amplitude values. d) Two-parameter phase values.

The identification process minimises the difference between the experimental and numerical DFT full-spectra. For this, the wear variables are modified until the values of the numerical forward (1x) and backward (-1x) components match the experimental values. Thus, it is possible to observe that the three-parameter model can practically reproduce a similar dynamic response than the two-parameter model due to its extra decoupled degree of freedom. However, the opposite is not possible. In general, the decoupling of the fault parameters enables a better phase identification.

When both wear models can represent the fault (Figure 7), either the identified wear severity and values of the 1x and -1x components agree with the physical wear and the experiments results. Nevertheless, one cannot correctly identify the parameters for situations in which the two-parameters can no longer reproduce the worn geometry. In these cases, the two-parameter model is not able to properly change the bearing dynamics in the same way as the physical wear, taken the same fault parameters. In these cases, a set of unrealistic parameters must be identified in order to accomplish the mathematical optimisation procedure.
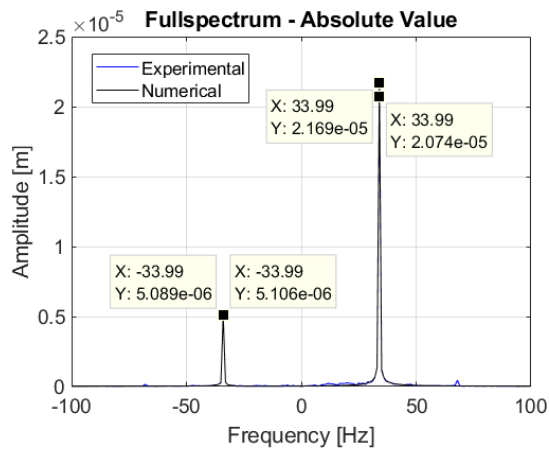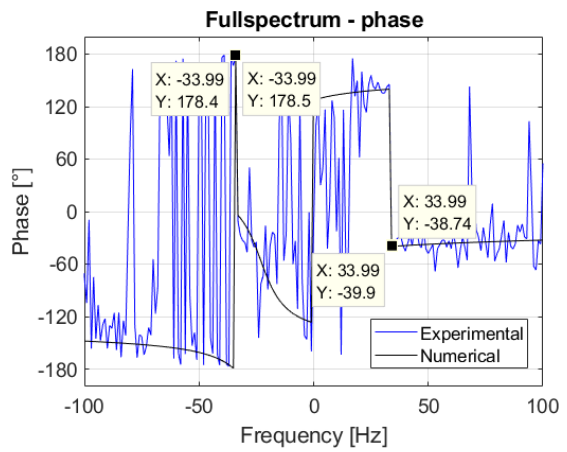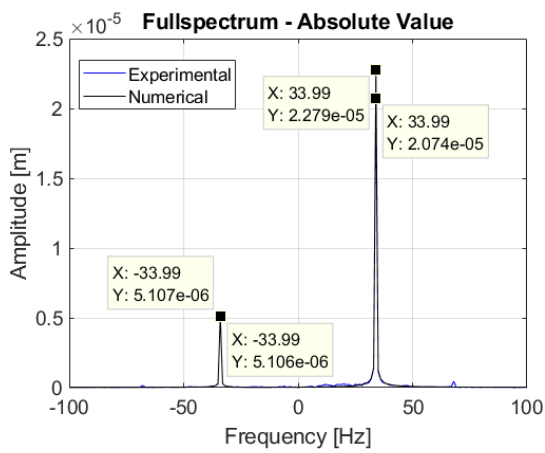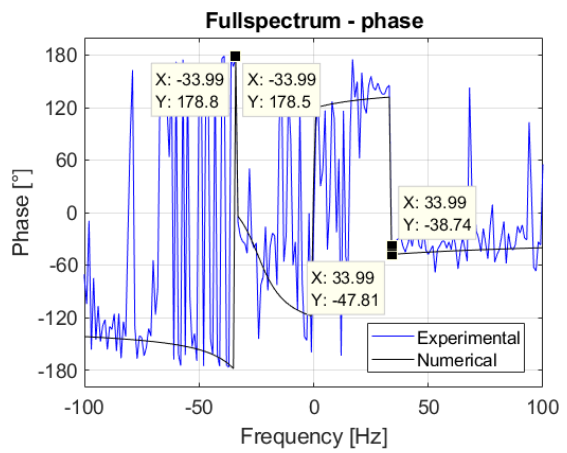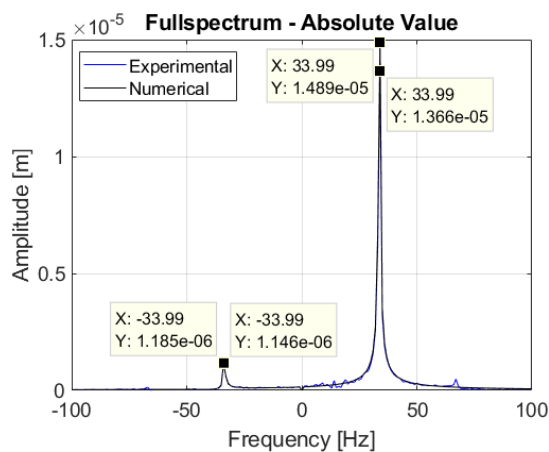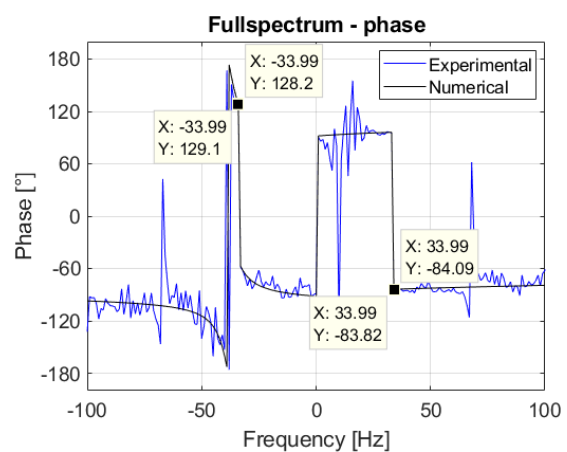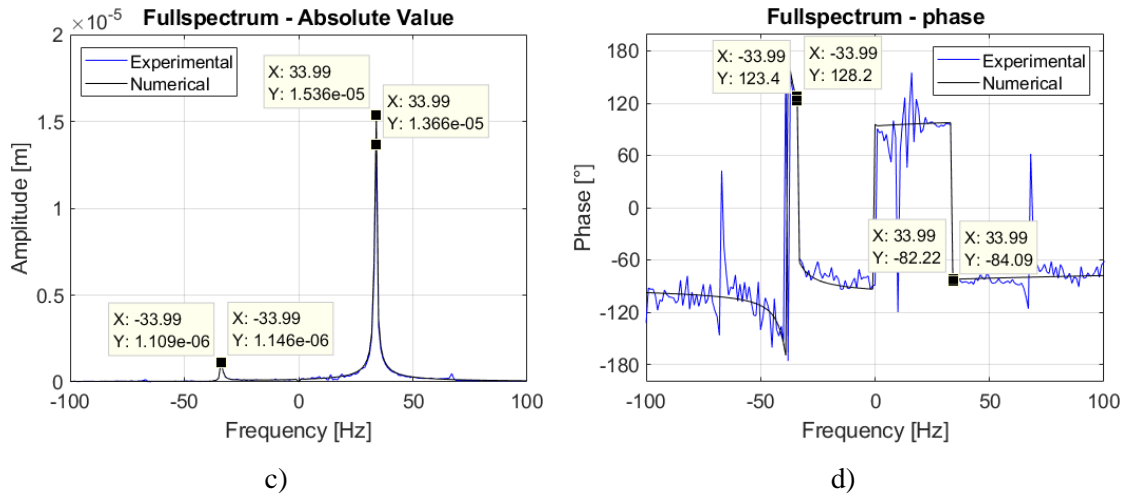
Figure 8 – Wear 2 DFT full-spectrum response: a) Three-parameter amplitude values. b) Three-parameter phase values. c) Two-parameter amplitude values. d) Two-parameter phase values.

c)   d)

Figure 9 – Wear 3 DFT full-spectrum response: a) Three-parameter amplitude values. b) Three-parameter phase values. c) Two-parameter amplitude values. d) Two-parameter phase values.

Therefore, it is interesting to note that the optimisation processes, using both wear models to compute the DFT full-spectrum, gives nearly the same spectral response for Wears 2 and 3, which can be seen by the 1x and -1x values of the DFT amplitude and phase (Figures 8 and 9). However, the parameters identified by each model are considerably different. As discussed previously, this fact indicates that the selection, or development, of a fault model that can correlate, both in geometry as in effect, to the physical one is mandatory. Otherwise, one will have mathematical parameters that satisfy the identification procedure; nevertheless, they may not resemble the physical fault.

5. Conclusions

The paper brings a discussion about a model-based identification of wear severity in journal bearings. For this, a rotating system supported on hydrodynamic and magnetic bearings was used. The identification was performed for three different machined wear geometries using two distinct wear models: a two-parameter model, in which the wear angular extent is proportional to its depth, and a three-parameter model, in which all fault parameters are independent of each other.

Since model-based identifications are based on minimising the differences between experimental and numerical responses, the entire process relies heavily on the precision of the mathematical model. Therefore, if the model can predict the physical behaviour with some accuracy, the wear identification can be successful, as presented in this work. However, if it is not possible to consider every dynamic effect in the numerical model, deviations between the identified and real parameters can be expected.

The small standard deviation obtained guarantees that the optimisation procedure is robust. Additionally, the standard deviation increases when the wear depth decreases, showing that shallow wear below a threshold is more difficult to identify precisely. However, since the dynamic behaviour of the rotor is not significantly affected by shallow wears, this fact is not a big concern in real applications. The algorithm is still able to monitor the wear severity even if the associated errors are slightly higher.

In addition, the identification process tries to match the numerical and experimental responses by selecting the wear parameters that minimise the objective function. When both wear models can represent the worn geometry and its effects in the rotating system, the selected parameters will usually meet expectations. If the wear model does not have good representativeness, the optimisation can still be accomplished with a good match between numerical and experimental responses. However, the identified fault parameters could have no resemblance to the physical ones. Therefore, it is mandatory to use a fault model that can reproduce the desired dynamic effects with the best fidelity in order to provide a robust and accurate estimation of the fault

20

criticality stage.

References

[1] Papadopoulos C. A., Nikolakopoulos P. G., Gounaris G. D., Identification of clearances and stability analysis for a rotor-journal bearing system, Mechanism and Machine Theory, vol. 43, p. 411-426, 2008.

[2] Gertzos K. P., Nikolakopoulos P. G., Chasalevris A. C., Papadopoulos C. A., Wear identification in rotor-bearing systems by measurements of dynamic bearing characteristics, Computers and Structures, vol. 89, p. 55-66, 2011.

[3] Jiang F., Wei L., Wang Z., Zhu Z., Fault severity estimation of rotating machinery based on residual signals, Advances in Mechanical Engineering, vol. 2012, p. 518468-1 518468-8, 2012.

[4] Yanusa-Kaltungo, A., Sinha, J. K., Nembhard A. D., A novel fault diagnosis technique for enhancing maintenance and reliability of rotating machines, Structural Health Monitoring, vol. 14, n. 6, p. 604-621, 2015.

[5] Wang, W., Forrester, B. D., Frith, P. C., A unified approach to detecting and trending changes caused by mechanical faults in rotating machinery. Structural Health Monitoring, vol. 15, n. 2, p. 204-222, 2016.

[6] Haneef, M.D., Randall, R.B., Peng, Z., Wear profile prediction of IC engine bearings by dynamic simulation, Wear, vol. 364-365, p. 84-102, 2016.

[7] Lee, D., Sun, K. H., Kim, B., Kang, D., Thermal behavior of a worn tilting pad journal bearing: Thermohydrodyanmic analysis and pad temperature measurement, Tribology Transactions, vol. 61, n. 6, p. 1074-1083, 2018.

[8] Alves D. S., Daniel, G. B., de Castro, H. F., Machado, T. H., Cavalca, K. L., Gecgel, O., Dias, J. P., Ekwaro-Osire, S., Uncertainty in deep convolutional neural network diagnostics of journal bearings with ovalization fault, Mechanism and Machine Theory, vol. 149, p. 1-16, 2020, DOI: https://doi.org/10.1016/j.mechmachtheory.2020.103835.

[9] Dufrane K. F., Kannel J. W., Mccloskey T. H., Wear of steam turbine journal bearings at low operating speeds, Journal of Lubrication Technology, vol. 105, p. 313–317, 1983.

[10] Hashimoto H., Wada S., Nojima K., Performance characteristics of worn journal bearings in both laminar and turbulent regimes – Part I: Steady-state characteristics" ASLE Transactions, vol. 29, p. 565-571, 1986.

[11] Fillon M., Bouyer J., Thermohydrodynamic analysis of a worn plain journal bearing, Tribology International, vol. 37, n. 2, p. 129-136, 2004.

[12] Nikolakopoulos P. G., Papadopoulos C. A., A study of friction in worn misaligned journal bearings under severe hydrodynamic lubrication, Tribology International, vol. 41, p. 461-72, 2008.

[13] Machado T. H., Cavalca K. L., Modeling of hydrodynamic bearing wear in rotor-bearing systems, Mechanism Research Communications, vol. 69, p. 15 -23, 2015.

[14] Chun S. M., Khonsari M. M., Wear simulation for the journal bearings operating under aligned shaft and steady load during start-up and coast-down conditions, Tribology International, vol. 97, p. 440 – 466, 2016.

[15] Sander D.E., Allmaier H., Starting and stopping behaviour of worn journal bearings, Tribology International, vol. 127, p. 478-488, 2018.

[16] Machado T. H., Alves D. S., Cavalca K. L., Investigation about journal bearing wear effect on rotating system dynamic response in time domain, Tribology International, vol. 129, p. 124 – 136, 2019.

[17] Machado T.H., Storti G.C., Nonlinear model for wear effects in hydrodynamic bearings applied to rotating systems. In: Lacarbonara W., Balachandran B., Ma J., Tenreiro Machado J., Stepan G. (eds) Nonlinear Dynamics of Structures, Systems and Devices. Springer, Cham, 2020, DOI: https://doi.org/10.1007/978-3-030-34713-0_55.

[18] Alves D.S., Fieux G., Machado T.H., Keogh P.S., Cavalca K.L., A parametric model to identify hydrodynamic bearing wear at a single rotating speed. Tribology International, vol. 153, p. 106640-1 106640-20, 2021, DOI: https://doi.org/10.1016/j.triboint.2020.106640.

[19] Arghir M., Alsayed A., Nicolas D., The finite volume solution of the Reynolds equation of lubrication with film discontinuities, International Journal of Mechanical Sciences, vol. 44, p. 2119-2132, 2002.

[20] Patankar, S. V., Numerical heat transfer and fluid flow, 1st Ed. Hemisphere Publishing Corporation, Washington, DC, 1980.

[21] Nordmann R., Vibration control and failure diagnosis in rotating machinery by means of active magnetic bearings, in: CISM Int. Cent. Mech. Sci. Courses Lect., p. 301–311, 2014, DOI: https://doi.org/10.1007/978-3-7091-1821-4_7.

[22] Cole, M.O.T., Keogh, P.S., Sahinkaya, M.N, Burrows, C.R., Towards fault-tolerant active control of rotor-magnetic bearing systems, Control Engineering Practice, vol. 12, p. 491-501, 2004, DOI: doi:10.1016/S0967-0661(03)00173-4.

[23] Dimitri, A.S., El-Shafei, A., Adly, A.A., Mahfoud, J., Magnetic actuator control of oil whip instability in bearings, IEEE Transaction on Magnetics, vol. 51(11), p. 1-4, 2015. DOI: 10.1109/TMAG.2015.2456030

[24] El-Shafei, A., Integrated Journal Bearing, U.S. patent number 10,954,999, 2021.

[25] Sarmah, N., Tiwari, R., Dynamic analysis and identification of multiple fault parameters in a cracked rotor system equipped with active magnetic bearings: a physical model based approach, Inverse Problem in Science and Engineering, vol. 28(8), p. 1103-1134, 2020, DOI: https://doi.org/10.1080/17415977.2019.1700982.

[26] Sun, J., Zhou, H., Ju, Z., Dynamic stiffness analysis and measurement of radial active magnetic bearing in magnetically suspended molecular pump, Scientific Reports, p. 1-16, 2020, DOI: https://doi.org/10.1038/s41598-020-57523-8

[27] Rutland, N.K., Keogh, P.S., Experimental validation of active magnetic bearing force characteristics, Report No. 032/1995, University of Bath, UK, 1995.

[28] Schweitzer, G., Maslen, E.H., Magnetic bearings: Theory, design, and application to rotating machinery, Springer-Verlag Berlin Heidelberg, 1st Ed., 535 p., 2009.

[29] Lalanne, M., Ferraris, G., Rotordynamics prediction in engineering, John Wiley & Sons, England, 266 p., 1998.

[30] Lund, J. W., Review of the concept of dynamic coefficients for fluid film journal bearings, ASME Journal of Tribology, vol. 109, p. 37- 41, 1987.

[31] Bazaraa, M. S., Sherali, H. D., Shetty, C. M., Nonlinear programming – Theory and algorithms, John Wiley and Sons, New Jersey, 2006.

[32] Dennis, J. E., Schnabel, R. B., Numerical methods for unconstrained optimization and nonlinear equations, Prentice-Hall, Philadelphia, 1996.

[33] Nocedal, J., Wright, S. J., Numerical optimization, Springer-Verlag, New York, 1999.

[34] Mendes, R. U., Machado, T. H., Cavalca, K. L., Experimental wear parameters identification in hydrodynamic bearings via model-based methodology, Wear, vol. 272-273, p. 116-129, 2017.